Osteogenic Differentiated Human Bone Marrow Stem Cells Contribute to Sprouting Angiogenesis Deceleration via Paracrine Excreted IGFBP7

Shiyu Sun, Cen Cao, Yaru Guo, Yi Hou, Yanze Meng, Yuman Li, Feng Mei, Zhewen Hu, Yao Li, Yuting Niu, Yiming Chen, Lili Chen,* Ying Huang,* and Xuliang Deng*

Deceleration of sprouting angiogenesis until its final disappearance after blood vessel reconstruction is crucial for controlled tissue repair; however, its underlying mechanism remains unclear. It is reported that osteogenic differentiated bone marrow stem cells (OD-BMSCs) contribute to sprouting angiogenesis deceleration by releasing intrinsic "OFF" signals. In vitro experiments show that insulin-like growth factor-binding protein 7 (IGFBP7) is the main component of OD-BMSCs paracrine products which could inhibit the tube formation ability of endothelial cells. In addition, cell functional experiments show that IGFBP7 inhibits sprouting angiogenesis by reducing cell migration and tip cell specification. Furthermore, it is found that early IGFBP7 intervention, which accelerates sprouting angiogenesis deceleration during the early stage of healing, impedes bone defect healing. These results demonstrate that OD-BMSCs could offer intrinsic inhibitory signals on sprouting angiogenesis and the appropriate emergence timing of these signals is crucial to maintain vasculature homeostasis during bone repairing. These results provide insight into the complex interaction between osteogenesis–angiogenesis coupling and suggest the potential therapeutic application of IGFBP7 in regulating vascular homeostasis.

1. Introduction

Sprouting angiogenesis is the formation of new capillaries out of the preexisting ones induced by hypoxia, soluble factors, and various biomechanical stimuli and is an aspect of normal healing process resulting in capillary bed formation.[1,2] However, sprouting angiogenesis can proceed as an overshooting reaction that results in the formation of additional blood vessels, followed by delayed decelerating growth.[3] This decelerating phase occurs simultaneously with the regression of superfluous vessels at a later stage of healing so that vessel beds are pruned back to normal vascular density and vascular homeostasis is maintained;[4] this process is particularly important because uncontrolled vessel growth leads to pathological effects such as proliferative diabetic retinopathy,[5,6] and incorrect vascular patterning causes vessel instability and poor network functionality.[7] Therefore, organized angiogenesis deceleration at the later stage of healing is crucial for vessel normalization and stabilizing the mature vessels, ensuring that tissue regeneration including bone defect healing can be carried out within a controllable range; however, the mechanism behind this remains unclear.

Alteration of extrinsic microenvironment, such as hypoxia improvement, is known as a common cause of capillary deceleration,[8,9] yet the decelerating angiogenesis response is usually accompanied by the repairing process of various injured tissue.[10] Therefore, it's reasonable to assume that intrinsic

S. Sun, Y. Guo, Y. Meng, Y. Li, Z. Hu, Y. Li, Y. Niu, Y. Chen,
Y. Huang, X. Deng
Beijing Laboratory of Biomedical Materials
Department of Geriatric Dentistry
Peking University School and Hospital of Stomatology
Beijing 100081, China
E-mail: kqhuangying@bjmu.edu.cn; kqdengxuliang@bjmu.edu.cn
C. Cao, F. Mei, L. Chen
Department of Stomatology
Union Hospital
Tongji Medical College
Huazhong University of Science and Technology
Wuhan 430022, China
E-mail: chenlili1030@hust.edu.cn

C. Cao, F. Mei, L. Chen
School of Stomatology
Tongji Medical College
Huazhong University of Science and Technology
Wuhan 430040, China
C. Cao, F. Mei, L. Chen
Hubei Province Key Laboratory of Oral and Maxillofacial Development
and Regeneration
Wuhan 430022, China
Y. Hou
College of Life Science and Technology
Beijing University of Chemical Technology
Beijing 100029, China

**ADVANCED
SCIENCE NEWS**
www.advancedsciencenews.com

**ADVANCED
MATERIALS
INTERFACES**
www.advmatinterfaces.de

signals from neighboring mature tissue assist in sprouting angiogenesis deceleration during bone defect healing as well. Bone mesenchymal stromal cell (BMSC) is a key player that serve as a multipotent functional cell-line to repair damaged tissues in bone defect healing site,[11] and BMSCs have a close spatial relationship with endothelial cells (ECs) physiologically.[12,13] Studies have demonstrated undifferentiated BMSCs can promote EC functions via the juxtacrine actions of ephrinB2/Ephs signaling pathways,[14] which indicates that BMSCs may support tube formation ability of ECs in the initial stage of bone defect. However, as BMSCs gradually differentiate into mature cells during the healing process, both the differentiated stage of BMSCs and the adjacent BMSC–EC relationship change. Therefore, we pondered whether osteogenic differentiated MSCs may contribute to the deceleration of sprouting angiogenesis by releasing "shut-off" signals to the growing neo-capillaries hypothetically.

In this study, we aimed to evaluate whether and how OD-BMSCs contribute to organized reduction in angiogenesis during bone defect healing. This study will deepen the existing knowledge on feedback regulation mechanisms of hBMSC-EC interactions in bone defect healing and suggest the potential therapeutic application of insulin-like growth factor-binding protein 7 (IGFBP7) in regulating angiogenesis and critical-size bone defects.

2. Results

2.1. Sprouting Angiogenesis Gradually Entered a Decelerating Stage Accompanied by New Bone Formation

MRI scan and CD31 immunohistochemical staining showed that the bone defect healing site initially received a robust and vigorous angiogenic response; yet the vascular network then decreased in number and fused into large vessels during the subsequent healing process (**Figure 1**A,B,D). Furthermore, micro-CT reconstruction of the cranial defect showed that new bone extended outward from the rim of the defect, reaching a plateau at 4 wk post-surgery (Figure 1C,E). Moreover, Masson's staining showed that the new bone (blue) in the defect area continuously mineralized into a mature bone (red; Figure S1A, Supporting Information), and immunohistochemical staining also showed that OCN and RUNX2 expressions peaked at 4 weeks post-surgery (Figure S1B,C, Supporting Information). Thus, it is clear that during natural bone defect healing, with continuous formation and maturation of new bones, sprouting angiogenesis gradually decelerates, implying that maturation of newly formed bones may contribute to sprouting angiogenesis deceleration (Figure 1F).

2.2. IGFBP7 Mediated the Angiogenic Inhibition Effects of Osteogenic Differentiated hBMSCs

Primary human umbilical vein endothelial cells (hUVECs) were used to verify the role of OD-BMSCs on ECs.[15] The administration of conditioned medium (from hBMSCs after 1/3/7 days of osteogenic induction) inhibited the tube formation ability of hUVECs, which was the lowest in OI 7 d group (**Figure 2**A,C,D). This finding confirmed that OD-BMSCs negatively regulate the tube formation ability of hUVECs via paracine secretion.

Tandem mass tag proteomic analysis was used to identify the specific components of paracrine OD-BMSC products that inhibited angiogenesis (Figure 2B and Figure S2, Supporting Information). The database was collated and we focused on IGFBP7, which is functionally related to angiogenesis and microtubule cytoskeleton organization, yet its specific role in vascular remodeling remains unclear. Later, qPCR and ELISA experiments confirmed that IGFBP7 secretion gradually increased with the development of osteogenic differentiation in hBMSCs (Figure 2E,F). Furthermore, to confirm whether other paracrine products of OD-BMSCs are involved in negative regulation of the tube formation ability of hUVECs, IGFBP7 expression was silenced via RNA interference. We found that IGFBP7 silencing in hBMSCs rescued the inhibitory effect of OD-BMSCs on hUVECs (Figure 2G–J). Therefore, these results confirmed IGFBP7 as a main component of paracrine OD-BMSC products that inhibited sprouting angiogenesis. Tube formation assay (Figure 2K–N) and subcutaneous transplantation assay (Figure 2O–R) showed that IGFBP7 inhibiting sprouting angiogenesis in a concentration-dependent manner.

2.3. IGFBP7 Inhibited EC Sprouting Angiogenesis by Regulating Cellular Cytoskeleton Organization

Directional migration of EC is crucial for the expansion of the newly formed vascular system, which determines the outcome of angiogenesis.[16] To further explore the possible mechanism by which IGFBP7 affects hUVECs, we analyzed the changes in the proteomics of hUVECs stimulated by different concentrations of IGFBP7. Differentially expressed proteins were classified by gene ontology and indicated that proteins functionally related to cell movement and cellular cytoskeleton organization exhibited significant changes (Figure S4, Supporting Information). Therefore, Cell-IQ live image monitoring system and wound healing assay was performed to evaluate the motility and migration of hUVECs. We found that the cell trajectory length in the IGFBP7-stimulated group was significantly lower than that in the control group (**Figure 3**A,B), and IGFBP7-stimulated hUVECs migrated slower toward the middle part of the wound compared to control (Figure 3C,D). These findings indicated that IGFBP7 inhibited the migration of ECs from existing vessels during bone defect healing.

Cell polarity is crucial for directional EC migration.[17] Positioning of the Golgi apparatus dictates the directionality of the proper localization of polarity cues in polarized cells.[18] Hence, we further assessed the orientation of Golgi apparatus in the leading edge of the migrating ECs to analyze EC polarity.[19,20] After IGFBP7 stimulation at a dose of 160 ng mL^{-1} for 12 h, ECs at the leading edge of the wound healing assay displayed randomly positioned Golgi apparatus and microtubule organizing centers including microtubules (shown by tubulin), whereas ECs in the absence of IGFBP7 displayed an arrangement of Golgi apparatus position that was coincident with the direction of cell migration (Figure 3E). Polar plots determining the center of mass of
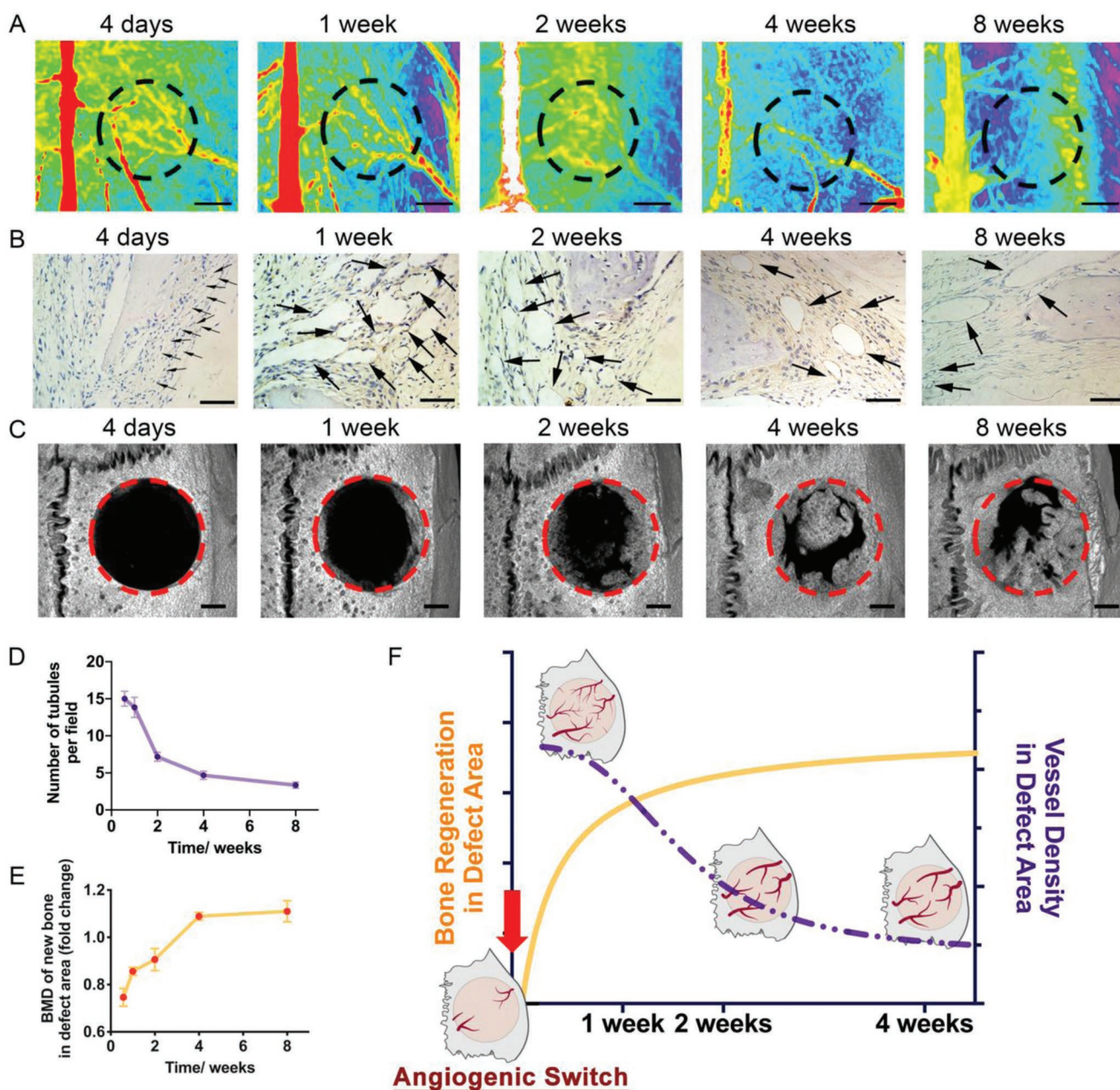
**ADVANCED
SCIENCE NEWS**

www.advancedsciencenews.com

**ADVANCED
MATERIALS
INTERFACES**

www.advmatinterfaces.de

Figure 1. Sprouting angiogenesis tended to plateau over time accompanied by new bone formation. A) Representative images of MRI scanning demonstrated neo-capillary regeneration after cranial bone defection surgery over time. Scale bar: 2 mm. B) Immunohistochemistry of CD31 showed that the number of small vessels of the regenerated new bone reduced 1 week after cranial bone defection surgery. Blood vessels marked by CD31 were indicated in brown. Scale bar: 100 μm. C) Representative images of micro-CT demonstrated new bone regeneration after cranial bone defection surgery over time. Scale bar: 1 mm. D) Histomorphological quantification of blood vessels mm^{-2} in (B). Data were presented as mean ± SEM of six independent experiments. E) The bone mineral density (BMD) of the regenerated new bone plateaued, increasing 4 weeks after cranial bone defection surgery. F) Fitted curves with bone mineral density of the new bone and the vessel density in the defect area were created and presented in a dual-axis chart to visually illustrate that the new bone formation and blood vessel remodeling were two biological processes with opposite trends.

the Golgi apparatus and microtubule organizing centers in relation to the center of mass of the cell nucleus provided a visual representation of the front–rear polarity of migrating cells (Figure 3F,G). These data indicated that 160 ng mL^{-1} of IGFBP7 negatively regulated endothelial polarity, resulting in decreased hUVEC directional migration.

Ingenuity pathway analysis of the proteomic result showed that calpain proteins, which are functionally related to cellular cytoskeletal changes,[21,22] might be the downstream effector proteins that affect EC migration and polarity (Figure S4, Supporting Information). qPCR and western blotting results showed that Calpain-1 and Calpain-2 expression increased
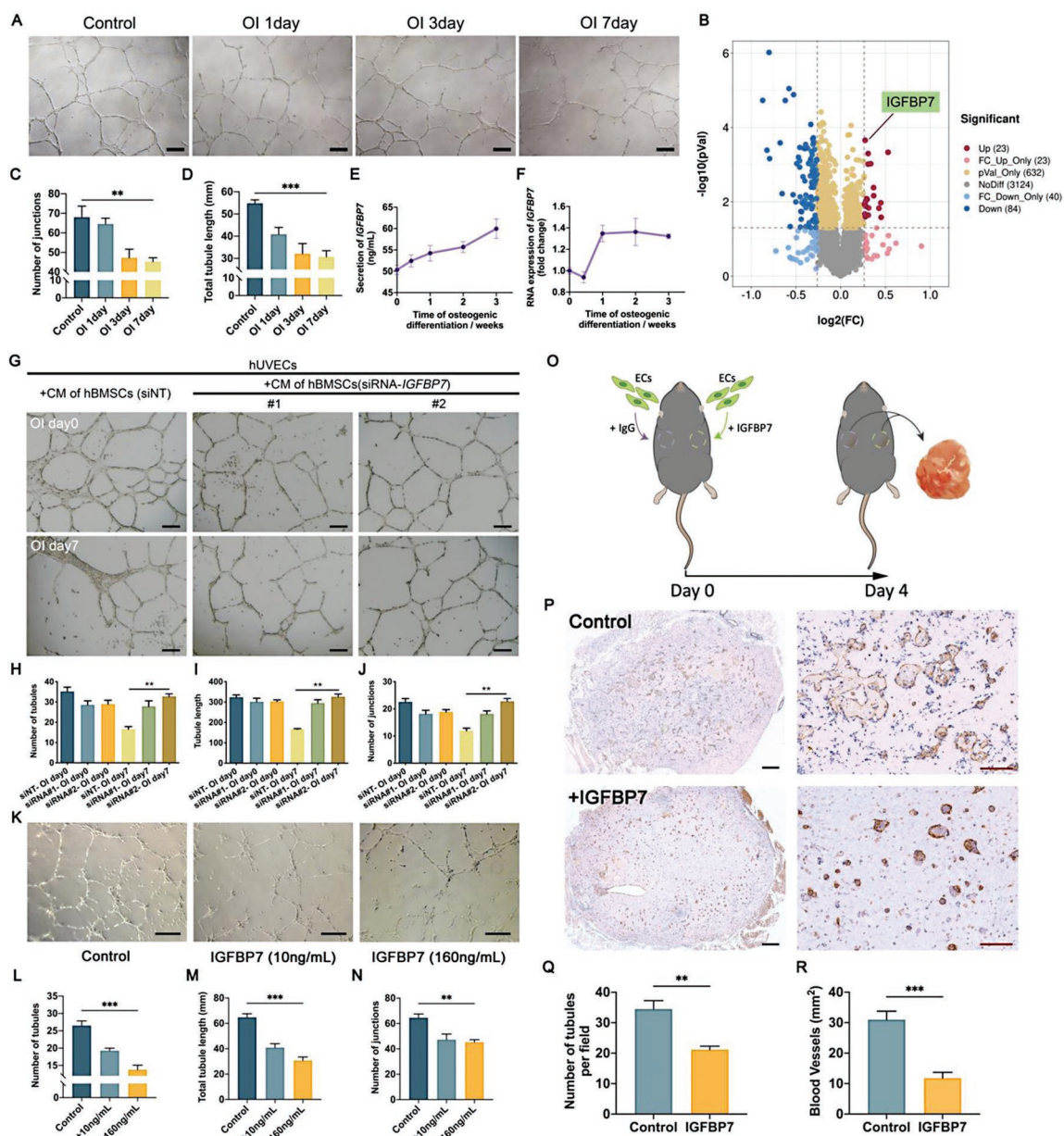
Figure 2. IGFBP7 mediated the angiogenic inhibition effect of paracrine products of OD-hMSCs on ECs. A) Representative images of tube formation at 8 h after cells were seeded on Matrigel. Control group: hUVECs cultured in 1:1 endothelial cell medium and osteogenic induction medium. OI 1/3/7 d group: hUVECs cultured in 1:1 endothelial cell medium and conditioned medium of hBMSCs under osteogenic induction for 1/3/7 days. Scale bar: 200 μm. B) Volcano plots showing the distribution of significance and fold change of identified proteins in MSCs between 0 and 7 days post-osteogenic induction. The red and blue spots indicate significantly upregulated and downregulated proteins, respectively. C,D) Total tube length and the number of junctions in each group in (A) at 8 h were quantified using Image Pro Plus software. E) ELISA results showed that IGFBP7 secretion by hBMSCs increased with the prolongation of osteogenic induction. Data were presented as mean ± SEM of three independent experiments. F) qPCR assay confirmed that mRNA expression of IGFBP7 of hBMSCs increased with the prolongation of osteogenic induction. OI 0/3/7/14/21 d: hBMSCs under osteogenic induction for 0/3/7/14/21 days. Data were presented as mean ± SEM of three independent experiments. G) Representative images of tube formation at 8 h after hUVECs were seeded on Matrigel cultured in 1:1 endothelial cell medium and conditioned medium of hBMSCs transfected with non-targeting siRNA (siNT) or siRNA-IGFBP7#1/2. OI 0/7 d: hBMSCs under osteogenic induction for 0/7 days. Scale bar: 200 μm. H–J) Total tube length, number of tubules, and number of junctions in each group in (F) at 8 h were quantified using Image Pro Plus software. Data were presented as means ± S.E.M. of three independent experiments. K) Representative images of tube formation at 8 h after cells were seeded on Matrigel. When hUVECs were directly stimulated by IGFBP7, we observed that the total tube length and the number of junctions and tubules decreased with the increase in concentration of IGFBP7. Scale bar: 150 μm. L–N) Total tube length and number of tubules and junctions in (K) at 8 h were quantified using Image Pro Plus software. O) Schematic illustration of IGFBP7 application in nude mice with xenograft. P) Representative images of subcutaneous transplantation of hUVECs in nude mice with or without IGFBP7 (160 ng mL^{-1}) for 4 days observed using CD31 immunohistochemistry marking of blood vessels. It's shown that IGFBP7 group displayed fewer vascular tubules and a smaller range of blood vessel area than the control group. Black scale bar: 500 μm. Brown scale bar: 200 μm. Q,R) Number of tubules per field and the area of blood vessels in (P) were quantified using Image Pro Plus software.
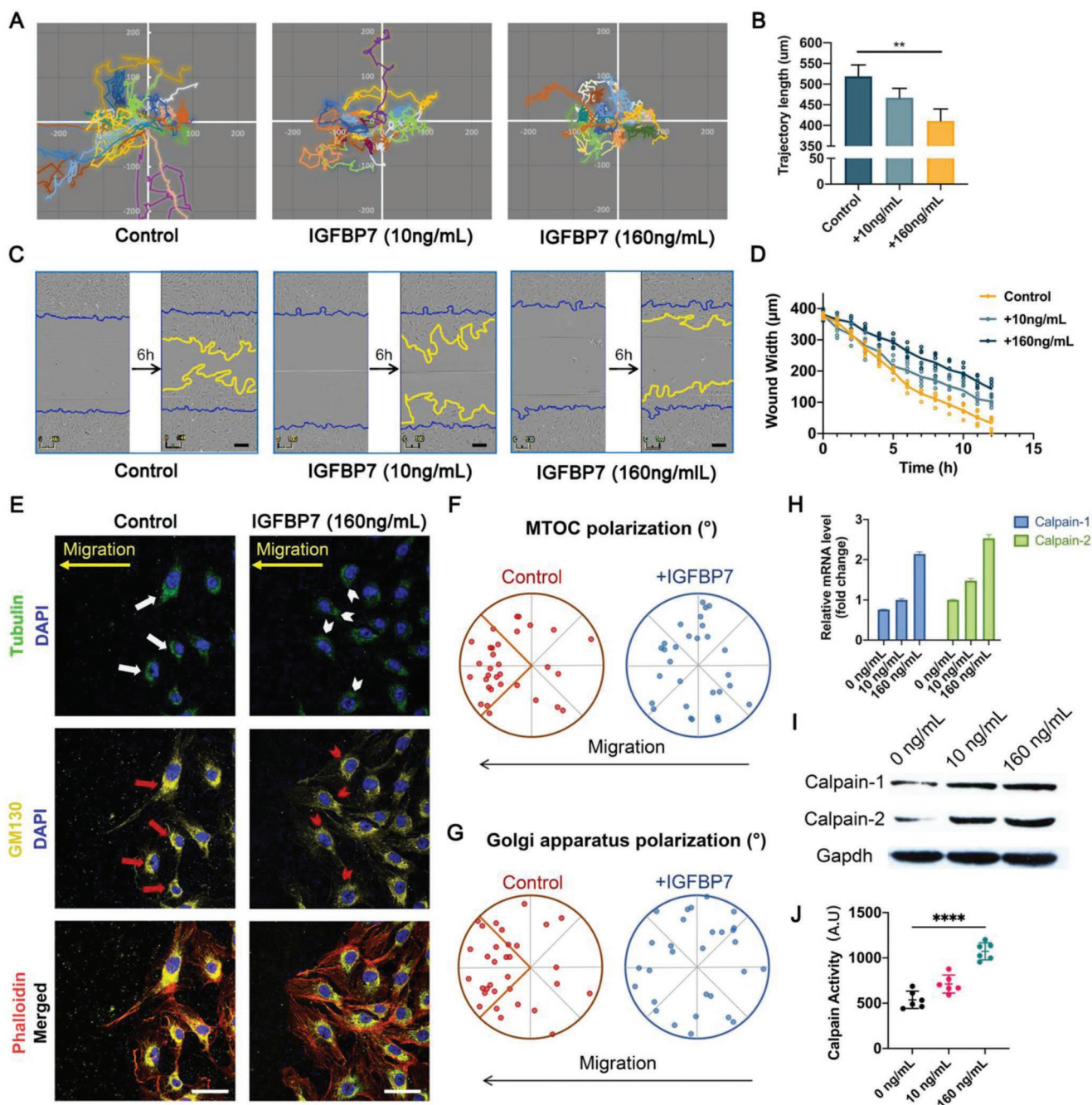
**ADVANCED
SCIENCE NEWS**

www.advancedsciencenews.com

**ADVANCED
MATERIALS
INTERFACES**

www.advmatinterfaces.de

Figure 3. IGFBP7 negatively regulated cell polarity in ECs migration. A) Representative micrographs of hUVEC wound healing with or without IGFBP7 stimulation at doses of 10 and 160 ng mL^{-1}. Scale bar: 100 μm. B) Quantification analysis of hUVEC wound healing process based on wound width. C) Dynamic alterations of cell movement with or without IGFBP7 stimulation at doses of 10 and 160 ng mL^{-1} observed using the Cell-IQ Alive Image Monitoring System. D) Representative images of tube formation at 8 h after cells were seeded on Matrigel. Scale bar: 150 μm. E) Representative images of phalloidin + actin cytoskeleton, α-tubulin + microtubule, GM130 + Golgi apparatus, and DAPI in the leading edge of ECs at 12 h after initiation of cell migration with or without IGFBP7 stimulation at a dose of 160 ng mL^{-1}. Note that the microtubule and Golgi apparatus (white and red arrows) in the control group were localized in the direction of cell migration, while those (white and red arrowheads) in ECs stimulated by IGFBP7 were randomly localized. Scale bar: 50 μm. F) Polar plots showing the microtubule organizing center (MTOC) polarization [$n = 32$ (control), 29 (IGFBP7)]. G) Polar plots showing Golgi apparatus polarization [$n = 32$ (control), 29 (IGFBP7)]. Data were presented as mean ± SEM of three independent experiments. H) qPCR results showed that mRNA expression of calpain-1 and calpain-2 increased in hUVECs after IGFBP7 stimulation. I) Western blotting results showed that calpain-1 and calpain-2 expression increased in hUVECs after IGFBP7 stimulation. J) Calpain activities of hUVECs increased after stimulation by 10 ng mL^{-1} or 160 ng mL^{-1} of IGFBP7.

with an increase in IGFBP7 concentration (Figure 3H,I). Furthermore, the calpain activity assay showed that IGFBP7 significantly increased the calpain activity of hUVECs at a dose of 160 ng mL^{-1} (Figure 3J). These results confirmed that IGFBP7 inhibited EC migration by negatively regulating cell polarity and that calpain series proteins were possible downstream effector proteins.

2.4. IGFBP7 Inhibited Endothelial Tip Cell Formation In Vitro and In Vivo

Generally, angiogenesis occurs from the pre-existing vasculature by sprouting ECs.[23] Once initiated, outgrowing capillaries are spearheaded by specialized ECs, termed tip cells, followed by stalk cells and endothelial tip specification is known as a major control point in angiogenesis.[24] In this study, we tried to explore whether IGFBP7 negatively regulates sprouting angiogenesis by affecting endothelial tip-cell specification.

To confirm the role of IGFBP7 in tip cell specification, a spheroid-based three-dimensional angiogenesis assay was adopted.[25,26] We found that IGFBP7-stimulated hUVEC spheroids exhibited less extension and decreased invasion distance into the matrix (**Figure 4**A,B). Furthermore, mRNA levels of tip cell-enriched gene transcripts, including CD34, VEGFR-2, CXCR4, and EFNB2,[27–29] decreased in IGFBP7-stimulated hUVECs (Figure 4C) compared to the control group, so were the protein expression levels (Figure 4D). In addition, the results of flow cytometry showed that IGFBP7-stimulating hUVECs displayed a lower percentage of CD34$^+$ cells than the control group (Figure 4E,F). Thus, these data indicated that IGFBP7 inhibited the tip-cell specification of hUVECs in a concentration-dependent manner.

Developing mouse retina is an extensively used model to demonstrate endothelial tip specification in vivo.[30] Hence, we injected IGFBP7 (0.3 μg) directly into the eyes of 4 days post-natal mice, and the eyeballs were harvested after 2 days (Figure 4G). We found that IGFBP7 administration markedly inhibited retinal angiogenesis, resulting in fewer tip cells, fewer filopodia extensions at the vascular front and a significant reduction in the area covered by blood vessels, thereby indicating severe patterning defects in retinal vessels (Figure 4H,I). The aforementioned results confirmed that IGFBP7 inhibited tip cell specification of ECs both in vitro and in vivo.

2.5. Early Intervention of IGFBP7 Impeded Bone Healing and Angiogenesis in Cranial Bone Defect

To determine natural secretion of IGFBP7 in vivo, immunohistochemical staining was performed, which showed that IGFBP7 secretion peaked at week 2 of bone defect healing (**Figure 5**A,B). Thus, we pondered if early addition of exogenous IGFBP7 to shift the peak timepoint of IGFBP7 before week 2 would influence sprouting angiogenesis and bone formation. Hence, we injected IGFBP7 and IgG (as control) into the rat cranial bone defect sites 4 days post-surgery, shifting the peak time point of IGFBP7 to an earlier stage of healing (Figure 5C,D). In addition, vascular regeneration outcome was visualized using MRI 1

week post-injection (Day 11), and we evaluated the bone healing outcome by micro-CT 8 weeks post-surgery. Moreover, MRI scan of the control group showed abundant vascular signals whereas that of the IGFBP7 group showed a distinct reduction in signals, confirming that addition of IGFBP7 inhibited neovasculature in the defect region (Figure 5E,F). Micro-CT scan of rat skulls showed less new bone formation within the 5-mm defect area in the treatment group than in the control group at both 4 and 8 weeks post-surgery (Figure 5G,H). This result confirmed that shifting the peak time point of IGFBP7 impedes bone healing and angiogenesis in cranial bone defects.

3. Discussion

Vasculature homeostasis is an equilibrium state that ensures optimal efficiency of blood vessel networks and matching blood supply to the metabolic needs of tissues that regenerate over time.[31] Deceleration of robust capillary growth is a crucial part of this dynamic equilibrium;[3,7] however, the underlying mechanism remains unclear. It is generally accepted that sprouting angiogenesis deceleration is caused by alterations in the extrinsic microenvironment, such as hypoxia improvement, shear stress, and pulsatile luminal pressure.[32–34] In this study, we focused on the intrinsic signals that may regulate sprouting angiogenesis deceleration and found that IGFBP7 inhibited sprouting angiogenesis in ECs. This phenomenon demonstrated that intrinsic signals from neighboring mature cells assisted in vasculature homeostasis during bone defect healing, which also implies that both the extrinsic microenvironment and intrinsic signals are required to trigger sprouting angiogenesis deceleration.

In this study, the candidate inhibitor IGFBP7 was screened from the paracine products of hBMSCs after 7 days of osteogenic induction. The secretory activity of osteogenic cells increases with the progression of osteogenic lineage differentiation and then decreases when the secreted extracellular matrix begins to mineralize. In addition, we found that the expression of the main transcription factors (RUNX2 and osterix) that trigger osteogenic lineage differentiation of BMSCs reached its peak value 7 days after osteogenic induction,[35] as well as alkaline phosphatase activity and Col1 expression (Figure S5, Supporting Information). These results are consistent with those of previous studies,[36,37] which also proved that the secretory activity of BMSCs reached its peak value at 7 days after osteogenic induction. Thus, it is appropriate to screen candidate intrinsic angiogenic inhibitors from the paracine products of BMSCs after 7 days of osteogenic induction.

Although IGFBP7 is a member of the IGFBP-rPs superfamily, its affinity for IGF-1 is typically lower than that of IGFBP1-6.[38] Furthermore, IGFBP7 is highly expressed in some cancer cell lines, invading tumor cells in colon cancer and cancer vasculature;[39,40] however, its role in angiogenesis remains unclear. In addition, IGFBP7 accumulates in capillary-like tubes of human vascular ECs in vitro and plays an inhibitory role against the stimulatory effect of VEGFA on angiogenesis.[38,41,42] However, a recent study demonstrated that IGFBP7 promotes EC angiogenesis via CD93.[43] Hence, whether and how IGFBP7 regulates the formation of functional
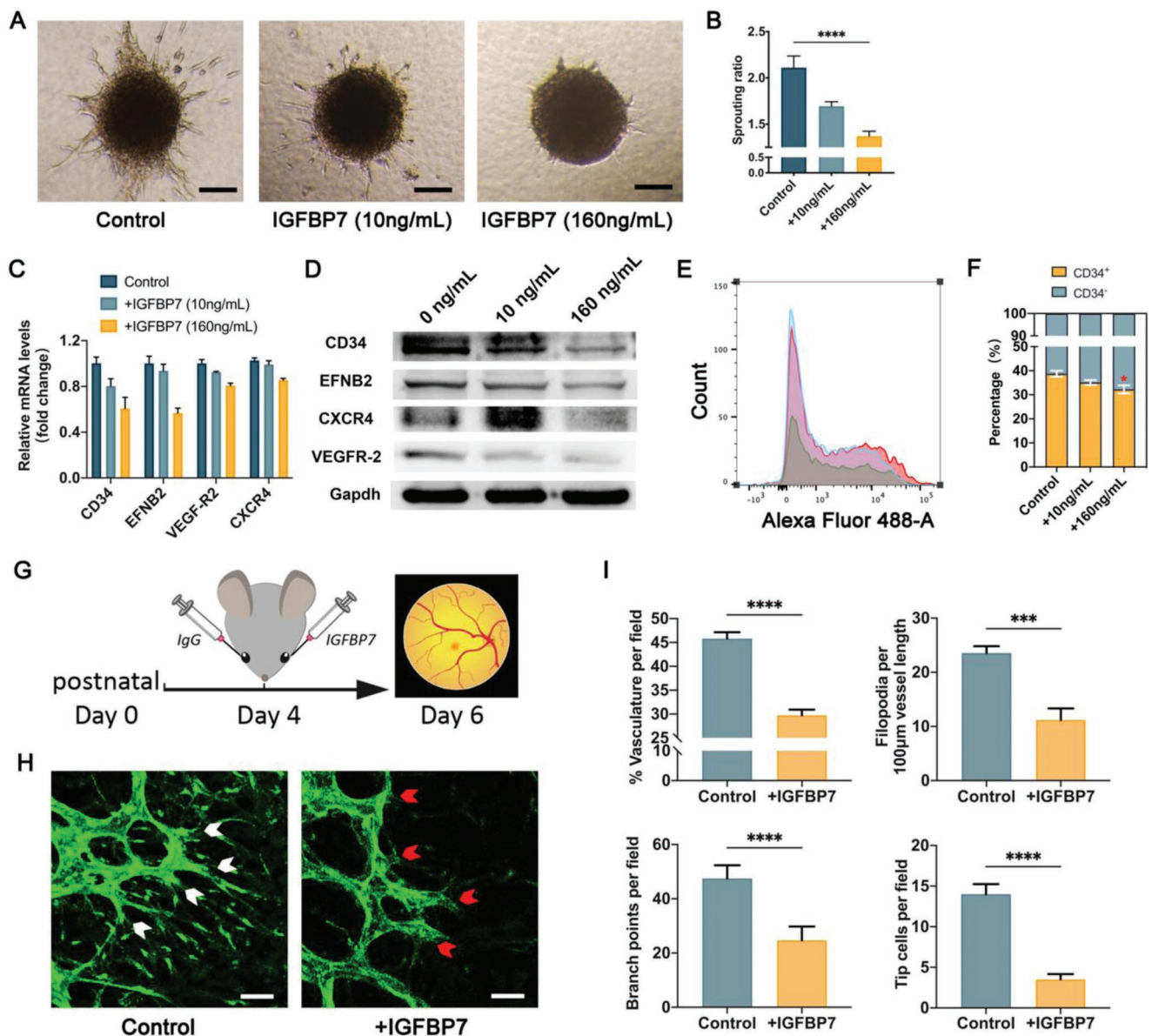
Figure 4. IGFBP7 inhibited endothelial tip cell formation in vitro and in vivo. A) Representative photomicrographs of 3D in vitro sprouting angiogenesis showed that IGFBP7 suppressed angiogenesis, exhibiting higher cellular invasion distance and numerous sprouts into matrices. Scale bar: 100 μm. B) Quantification analysis of the number of sprouts showed that there were statistically significant differences between the control group and hUVECs stimulated with 10 and 160 ng mL^{-1} of IGFBP7 (****$p < 0.001$). C) qPCR and D) western blotting showed that IGFBP7 reduced the expression of tip cell markers at both the mRNA (including CD34, VEGFR-2, CXCR4, and EFNB2), and protein levels (including CD34, VEGFR-2, CXCR4, and EFNB2). GAPDH was used as the internal control. E) Flow cytometry indicated that the percentage of CD34$^+$ cells was downregulated by IGFBP7. F) Quantitative analysis of tip cell contribution in both groups revealed that IGFBP7 inhibited the specification of hUVECs into tip cells. Data were presented as mean ± SEM of the three independent experiments (*$p < 0.05$). G) Scheme of IGFBP7/IgG administration in mice. H) Representative images of Isolectin B4 staining of the developing retinal vessels treated by IgG or 160 ng mL^{-1} showed that IGFBP7 treatment led to impaired retinal development with tip cell abnormalities. White arrows marked the filopodia of tip cells. Red arrows marked the absence of filopodia. Scale bar: 50 μm. I) Decreased branch points, tip cells, filopodia, and vasculature were observed after IGFBP7 treatment. Data were presented as mean ± S.E.M. of three independent experiments (***$p < 0.0001$).

vascular networks has remained unclear. In this study, we confirmed that IGFBP7 is an angiogenesis inhibitor that negatively regulates sprouting angiogenesis during tissue regeneration by inhibiting hUVEC migration and tip cell specification, which shows that reduced hUVEC migration after IGFBP7 stimulation can be attributed to its negative regulation of cell polarity.

Furthermore, previous studies have revealed that calpain series proteins are related to cell movement and modulate cell polarity,[21,22] while our results revealed that IGFBP7 upregulated calpain-1 and calpain-2 expression in hUVECs, which may explain how IGFBP7 negatively regulates cell polarity and results in reduced EC migration. Normal microtubule
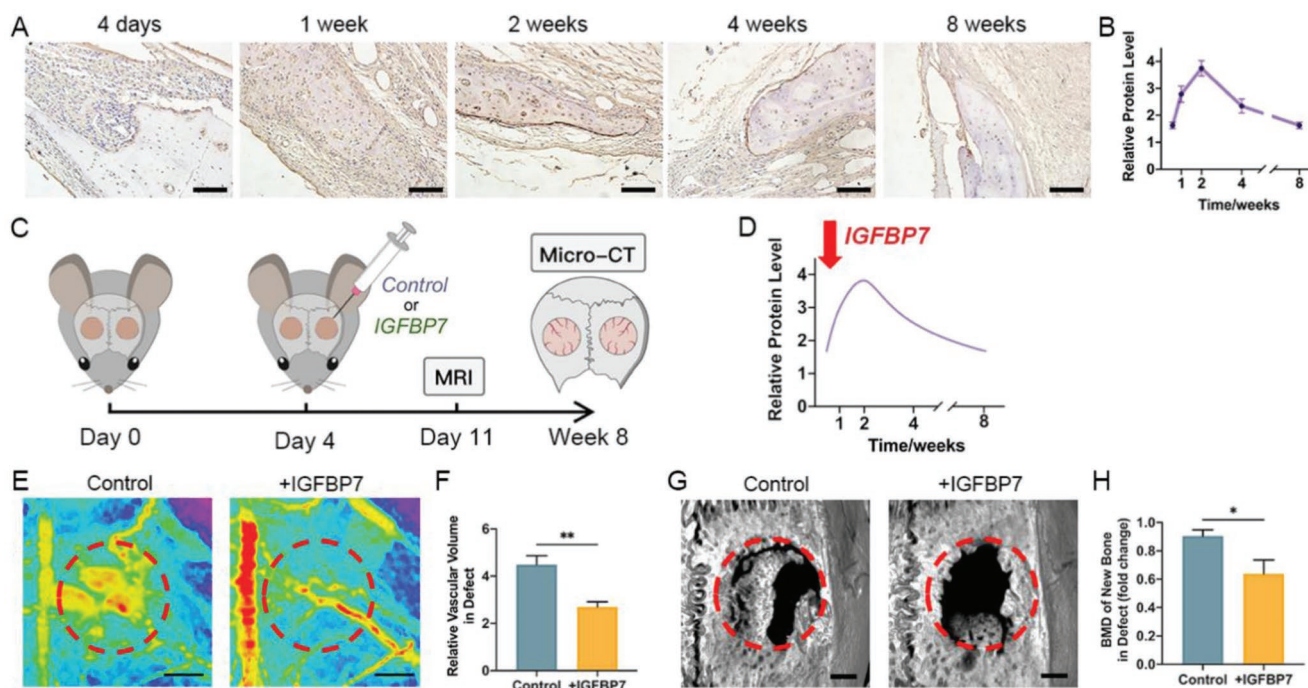
ADVANCED
SCIENCE NEWS
www.advancedsciencenews.com

ADVANCED
MATERIALS
INTERFACES
www.advmatinterfaces.de

Figure 5. Early intervention of IGFBP7 impedes bone healing and angiogenesis in cranial bone defect. A) Immunohistochemistry of IGFBP7 shows that IGFBP7 secretion reached maximum at 2 weeks after cranial bone defection surgery. Scale bar: 100 μm. B) Histomorphological quantification of relative OID of IGFBP7 per field. C) Scheme of IGFBP7/IgG administration in mice. D) Scheme of IGFBP7/IgG administration at 4 days post-surgery, shifting the peak time point of IGFBP7 to an earlier stage of healing. E) Magnetic resonance imaging (MRI) vessels visualizing the vessel networks in cranial defect area 1 week after IgG or IGFBP7 stimulation. Scale bar: 2 mm. F) Relative vascular volume at the site of the repair. Data were expressed as the mean ± SEM. * indicates significant difference ($p < 0.05$). $n = 4$. G) Micro-CT demonstrating regeneration of new bone 8 weeks after cranial bone defection surgery. Scale bar: 1 mm. H) When inducing early stimulation via IGFBP7 in the defect area, bone mineral density (BMD) significantly decreased. BMD was quantified by Inveon Research Workplace software.

functioning is essential for cell polarity, and an emerging view of cancer is that changes in regulation could contribute to several tumor cell capabilities.[44] Therefore, the aforementioned results suggest the potential therapeutic application of IGFBP7 in regulating vascular homeostasis.

Although this study highlights the realization of vascular homeostasis via extrinsic and/or intrinsic factors, obtaining adequate sprouting angiogenesis remains crucial at the initial stage of bone defect healing. Neocapillaries grow into the wound at a high rate post-surgery and produce abundant blood vessel networks, thereby improving the supply of oxygen, nutrients, and stem cells for sufficient tissue repair and metabolic waste removal.[45,46] Therefore, it is important to investigate temporal variations in the vascular sprouting process. In this study, we found that IGFBP7 peaked at 1–2 week post-surgery in vivo during normal defect healing, and its early intervention reduced sprouting angiogenesis in the early stage of bone defect healing and impeded the final bone formation quality (Figure 5). These findings further confirm that the appropriate time point of sprouting deceleration is crucial for maintaining the dynamic equilibrium of vascular remodeling, thereby affecting the final outcome of bone defect healing. In case of premature intervention, the initial establishment of the microvascular network will be damaged, which is detrimental to bone defect repair. This finding provides a novel basis for further discussion on vascularization strategies and various combinatorial therapies.

4. Conclusions

In summary, during natural bone defect healing, increased sprouting angiogenesis tended to stop, accompanied by continuous formation and maturation of new bones. In addition, we found that some signals that triggered sprouting angiogenesis deceleration were from the neighboring mature cells, such as differentiated BMSCs. Among these intrinsic signals, we screened out IGFBP7, which played a prominent role in mediating angiogenic inhibition effects on hUVECs in vivo and in vitro. Cellular analysis showed that IGFBP7 inhibited the angiogenic functions of hUVECs including cell migration and tip cell formation both in vitro and in vivo. Early intervention of IGFBP7 impeded the early stage sprouting angiogenesis, and the final bone healing suggested that the emergence timing of angiogenic inhibitors (such as IGFBP7) was crucial for vascular remodeling and tissue regeneration homeostasis. This study will deepen the existing knowledge on feedback regulation mechanisms of hBMSC–hUVEC interactions in bone defect healing and suggest the therapeutic potential therapeutic application of IGFBP7 in regulating angiogenesis and critical-size bone defects.

5. Experimental Section

Animals and Surgical Procedure: The animal surgical procedure was approved by the Institutional Animal Care and Use Committee of the Peking University (Approval number: LA2021378). Sixty male

**ADVANCED
SCIENCE NEWS**

www.advancedsciencenews.com

**ADVANCED
MATERIALS
INTERFACES**

www.advmatinterfaces.de

Sprague-Dawley (SD) rats (8 weeks old), 24 male C57BL mice (8 weeks old), and 24 male BALB/c nude mice (4 weeks old) were purchased from Beijing HFK Bioscience Co. Ltd. (Beijing, China). To avoid skewing the experimental data by sex and estrus cycle,[47] only male animals were used in this study.

To establish cranial defect models, forty 8-week-old male SD rats were used. The dorsal cranium was surgically exposed after the rats were anesthetized via intraperitoneal injection of phenobarbital sodium (100 mg kg^{-1}). A critical-sized full-thickness bone defect (5 mm in diameter) on the right side of the parietal bone was created using a saline-cooled trephine drill. Five model groups ($n = 8$) were established, and calvaria samples from each group were harvested at different time points post-surgery: 4 d, 1 wk, 2 wk, 4 wk, and 8 wk. The samples were then harvested and fixed in 4% (w/v) paraformaldehyde for 24 h at 24 °C. Subsequently, the specimens were examined using a high-resolution Inveon microtomography (Siemens, Munich, Germany). The bone volume was analyzed, and 3D reconstruction was performed based on the processed images using Scanco software. Following micro-CT analysis, the rat skulls were decalcified and paraffin-embedded. Subsequently, histomorphological analysis was performed on 5-µm-thick histological sections of the central part of the skull defect, which were then subjected to Masson's trichrome staining as per manufacturer's protocols. Further, images were captured using a Leica M205C microscope (Leica Microsystems, Heerbrug, Switzerland). Histological images were measured and analyzed using Image Pro Plus (Media Cybernetics, USA).

To evaluate the effects of IGFBP7 on angiogenesis in vivo, nude mice ($n = 6$ in each group) were subcutaneously administered with 1×10^7 hUVECs mixed with 0.1 mL of Matrigel (Becton, Dickinson and Company, Franklin Lakes, NJ, USA) at 4 °C on ice; the experimental group ($n = 6$) was administered with 100 µL of 50 µg mL^{-1} IGFBP7 (1334-B7, R&D Systems, MN, USA), and the control rats were administered with IgG. The implants were then harvested after 4 d.

For retinal vessel formation in vivo, 0.5 µg of IGFBP7 was administered intravitreally into one eye of a P4 neonatal C57BL/6N mouse, and 0.5 µg of IgG as control was administered into the other eye. Eyeballs were harvested two days later. Flat-mounted fixed tissues were stained with FITC-conjugated isolectin B4 and imaged using a confocal laser scanning microscope (Leica Microsystems, Heerbrug, Switzerland). Then, vasculature percentage, branch points, tip cell numbers, and filopodia were quantified using ImageJ software.

Twenty 8-week-old male SD rats with double-sided critical-sized full-thickness bone defects were established as previously described to explore the effects of IGFBP7 on angiogenesis in the defect area. Four days after surgery, 2 µg of IGFBP7 or IgG (control) was injected into newly created rat cranial defects ($n = 10$ in each group). After one week, the rats were subjected to magnetic resonance imaging (MRI) scan. Eight weeks after surgery, the whole calvariae were harvested for histological analysis.

Micro-Computed Tomography Analysis: The calvaria sections were collected and the soft tissues were removed. Then the samples were scanned using a micro-computed tomographic system (GANTRY-STD CT 3121; Siemens, Knoxville, TN) with 80 kV, 500 mA, a pixel size of 33.658 mm, a camera exposure time of 1500 ms, and 360 rotations around the vertical axis with a 1 rotation step. The aluminum filter was set at 0 mm during the scans. Raw data obtained at the scanning stage were reconstructed using the Inveon Research Workplace 4.2 software (Siemens).

MRI Scanning: For MRI scanning, rats were anesthetized with isoflurane (RWD, Shenzhen, China) in oxygen; the isoflurane dosage was 5% for induction and ≈2.5% for maintenance, which was delivered via a nose cone during the imaging sessions and controlled using an anesthesia system (RC2 Rodent Circuit Controller; VetEquip, CA, USA). A NaGdF$_4$@PEG probe provided by College of Life Science and Technology, Beijing University of Chemical Technology was used to obtain strong MR contrast enhancement effects;[48] the NaGdF$_4$@PEG probe was bolus-injected intravenously through the tail vein with a dose of 15 mg kg^{-1}, and images were acquired at 2 h post-injection. MRI was performed on a 7.0 T MRI system (BioSpec70/20 USR, Bruker, Karlsruhe, Germany) using a DCE-FLASH imaging sequence. The imaging parameters were set as follows: field of view = 3.0 × 3.0 cm^2, matrix size = 220 × 220; slice thickness = 0.25 mm; echo time = 1.5 ms; repetition time = 12.4 ms; and number of excitations = 3.0. T1 maps were calculated by pixel-wise fitting of repetition time-dependent signal intensity changes to a single exponential function. The spatial resolution of Micro-MRI was 0.1 mm.

Immunohistochemistry: Rat skulls were decalcified, and transplants were obtained 4 d post-surgery, which were then fixed with 4% paraffin for more than 24 h. Next, the samples were embedded in paraffin, and 5-mm-thick sections were prepared. After deparaffinization and subsequent rehydration, antigen retrieval was performed by boiling citrate antigen retrieval solution (P0081; Beyotime, Shanghai, China) for 20 min. Then, endogenous peroxidase activity was blocked with 3% H$_2$O$_2$ for 15 min. Subsequently, the samples were pre-blocked with 5% bovine serum albumin (BSA) (A1933; Sigma-Aldrich, Darmstadt, Germany) for 1 h at 24 °C and incubated with primary antibodies overnight at 4 °C, which were again incubated with HRP-labeled goat anti-rabbit IgG (H.L; A0208; Beyotime) for 1 h at 24 °C. The signal was detected using a DAB Horseradish Peroxidase Color Development Kit (P0203; Beyotime) for 5 min at RT. Hematoxylin counterstaining was performed for 2 min at RT. The slides were then covered with Kisser's mounting medium (C0181; Beyotime). The following primary antibodies and reagents were used for immunohistochemical analysis: anti-CD31 (ab28364), anti-osteocalcin (ab198228), anti-RUNX2 (ab192256), and anti-IGFBP7 (ab171085), which were purchased from Abcam (Cambridge, UK).

Cell Culture and Conditioned Medium Collection: Two human primary cell lines, hBMSCs and hUVECs, were purchased from ScienCell Research Laboratories (Carlsbad, CA, USA) and cultured in a mesenchymal stem cell medium (MSCM; 7501; ScienCell Research Laboratories) and endothelial cell medium (ECM; 1001; ScienCell Research Laboratories), respectively, in a humidified chamber with 5% CO$_2$ at 37 °C. The cells for all experiments were used at passages 3–6. For osteogenesis induction, hBMSCs were cultured in an osteogenesis induction medium (HUXXC-90021. Cyagen Biosciences, Guangzhou, China).

To perform indirect co-culture and analyze the secretome, cell medium (CM) was recovered from the cells cultured in fetal bovine serum-free basal medium during the last 24 h. For functional experiments with CM, normal hBMSCs and hUVECs (passages 6–8) were used, and CM was mixed with ECM at 1:1 ratio for indirect coculture with hUVECs. Subsequently, recombinant human IGFBP7 (1334-B7, R&D Systems) was added to the cell culture at the indicated final concentrations and incubated for 3 d.

In Vitro Tube Formation Assays: Under sterile conditions, 24-well plates were coated with 350 mL of Matrigel per well without introducing air bubbles. The plates were incubated at 24 °C for at least 60 min to allow the Matrigel to rehydrate. Next, 1×10^5 hUVECs were plated on Matrigel. Finally, 300 mL of medium was added, and the 24-well plates were incubated at 37 °C in a 5% CO$_2$ air incubator. Tube structures were observed under a phase-contrast microscope after 4, 8, and 12 h.

Scratch Wound Healing and Cell Tracking: Both scratch wound healing and cell tracking assays were performed using a Cell IQ Live Cell Kinetic Imaging & Quantification System (CM Technologies, Colorado, USA). For the scratch wound healing assay, cells were seeded at a density of 2×10^5 cells per well (in 24-well plates), and a scratch was made on the cell monolayer after 12 h. After washing the cells three times with serum-free medium, they were placed into the Cell IQ system and were observed for another 24 h. For cell tracking, the cells were seeded at 3000 cells per well (in 24-well plates) for 5 h prior to transfer into the Cell IQ system, and all the wells were imaged for every 12 min. The images were analyzed using a Cell IQ analyzer. To avoid proliferation effects, a serum-free culture medium was used for scratch wound healing and cell tracking assays.

Immunofluorescence Analysis: The samples were rinsed with phosphate-buffered saline (PBS) and fixed in 4% (w/v) paraformaldehyde for 15 min. Then, the samples were washed three times with PBS for 5 min each and were permeabilized with 0.1% (w/v) Triton X-100 (diluted with PBS) for 10 min and blocked with 3% (w/v) BSA (diluted

with PBS) for 1 h to minimize non-specific staining. After removing the permeabilization solution, the samples were rinsed and washed with PBS. These procedures were carried out at 24 °C. Then, the samples were incubated with the primary antibody in 3% (w/v) BSA overnight at 4 °C. After thorough rinsing with PBS for excess antibody removal, the cells were incubated with pre-adsorbed secondary antibody for 1 h in the dark. 4′,6-Diamidino-2-phenylindole (DAPI; Sigma-Aldrich) was used to stain nuclei, and images of three random fields of vision were captured using a confocal laser-scanning microscope (Leica Microsystems, Heerbrug, Switzerland). Cells in each group were quantified using Image-Pro Plus, and GraphPad Prism 6.0 was used for statistical analysis. The following antibodies and reagents were used for immunofluorescence: rabbit anti-GM130 polyclonal antibody, Alexa Fluor 647 (PA1-077-A647), phalloidin, Alexa Fluor 488 (A12379), and Alexa Fluor 594 (A12381) antibodies were purchased from Thermo Fisher Scientific (Rockford, IL, USA), and anti-alpha tubulin antibody (ab18251), anti-collagen I antibody (ab138492), donkey anti-rabbit IgG H&L Alexa Fluor 594 (ab150080), goat anti-mouse IgG H&L Alexa Fluor 647 (ab150115), and goat anti-rabbit IgG H&L Alexa Fluor 488 (ab150077) were purchased from Abcam.

siRNA Transfection: All siRNAs encoding green fluorescent protein for IGFBP7 knockdown were purchased from GeneChem Co., Ltd. (Suzhou, China). hUVECs were transfected with an siRNA targeting IGFBP7 (siRNA#1/2) or a control siRNA (siNT) prior to initiation of differentiation, as well as during the differentiation process. Cells transfected with a non-targeting siRNA were used as controls. hUVECs were seeded in six well plates at a density of 3×10^5 cells per well one day prior to lentiviral transfection. Next, siRNA was added to the cell culture with 5 mg mL^{-1} of polybrene (GeneChem, Quebec, Canada) and incubated for 12 h. To ensure IGFBP7 inhibition during the seven days of osteogenic differentiation, siRNA transfection was performed again 72 h after the first round. The sequences of siRNA are listed in Table S1 (Supporting Information). mRNA levels of IGFBP7 significantly reduced at day 7 of osteogenic differentiation by 90% compared to control cells transfected with siNT (Figure S3, Supporting Information).

Generation of Endothelial Cell Spheroids: Agarose (2% w/v) was used to create a mold for EC spheroids while preventing the adhesion of cells to the mold surface. It was heated to form a melted solution and then added to a 3D Petri dish (Microtissues Inc., Providence RI, USA). After solidification, the agarose molds were placed in a six-well plate for cell culture. Then, 180 µL of the cell suspension was seeded onto each mold. Twenty minutes later, the culture medium was added and cellular aggregates were allowed to form for 24 h.

Spheroid-Based Sprouting Angiogenesis Model: For the in vitro sprouting angiogenesis assay, spheroids were generated overnight and then embedded in gelatin methacryloyl (GelMA) gels (EFL, Suzhou, China). After light curing, the culture medium was added. The spheroids were then allowed to sprout for 8 h. Then, in vitro sprouting was quantified digitally by measuring the number of extensions and length of the sprouts (calculated as cellular invasion distance) in each spheroid using the Image Pro Plus software and by analyzing 8–10 spheroids per experimental group.

Real-Time Quantitative PCR Analysis: Total RNA was extracted using TRIzol reagent (Invitrogen, Carlsbad, CA, USA) as per the manufacturer's instructions. Then, they were amplified using different primers. The quality and quantity of the obtained RNA were analyzed using a spectrophotometer (NanoDrop 8000; Thermo Fisher Scientific). The RNA was then reverse-transcribed into complementary DNA (cDNA) using a reverse transcription kit (Takara Bio Inc., Tokyo, Japan). Subsequently, quantitative real-time polymerase chain reaction (qPCR) was carried out using a SYBR Green PCR reagent kit (Roche, Germany) on an ABI QuantStudio 3 Real-Time PCR System (Applied Biosystems, Foster City, CA, USA). The primer sequences are listed in Table S2 (Supporting Information). All values were normalized to those of GAPDH.

Western Blot Analysis: The cultured cells were lysed with RIPA lysis buffer (Beyotime) supplemented with protease inhibitor cocktail (Thermo Fisher) on ice. Then, protein concentration was quantified using a BCA protein assay kit (Beyotime), and 6× SDS Sample Loading Buffer (P0015F; Beyotime) was added to the protein before heating at 100 °C for 5 min. Subsequently, the total protein extract (30 µg) was separated by 10% (w/v) sodium dodecyl sulfate polyacrylamide gel electrophoresis, and the proteins were transferred to a polyvinylidene difluoride membrane. Next, the membranes were blocked with 5% (w/v) skim milk and incubated with the primary antibody at 4 °C overnight, followed by incubation with a secondary antibody conjugated with horseradish peroxidase (HRP). Then, autoradiography was performed using an ECL Western Blot kit (CoWin Bio., Jiangsu, China) on a film-exposure machine. GAPDH was used as the protein loading control, and protein expression levels were normalized to those of GAPDH. The following antibodies were used: anti-GAPDH (ab9485), anti-IGFBP7 (ab171085), anti-CD34 (ab81289), anti-VEGFR2 (ab39256), anti-CXCR4 (ab181020), and anti-EphrinB2 (ab150411) were purchased from Abcam. The secondary antibody used was HRP-labeled IgG (A0208, A0216; Beyotime).

Flow Cytometry Analysis: Cell suspensions were obtained by pancreatin treatment of the adherent endothelial cell monolayers. Immunofluorescence labeling and washing were performed in PBS containing 0.1% (w/v) BSA. The cells were then fixed in 2% (w/v) paraformaldehyde in PBS for 15 min at 24 °C and incubated with the primary antibody anti-CD34 (ab81289; Abcam) diluted in 1% (w/v) BSA. Then, the cells were washed three times with PBS and probed with secondary antibodies (Alexa Fluor-488, ab150077; Abcam) for 1 h at 24 °C. Cell nuclei were stained with DAPI, and the cells were then washed three times with PBS and analyzed by flow cytometry on a FACSCalibur (Becton, Dickinson and Company) in combination with FlowJo software 10.4 (Tree Star, San Carlos, CA, USA).

Calpain Activity: Calpain activity was measured using a calpain activity kit (ab65308, Abcam) as per manufacturer's protocol. Briefly, the proteins from hUVECs were collected, and the protein concentration was determined using a protein assay kit (Bio-Rad, Hercules, CA, USA). Then, they (200 µg) were incubated in a 96-well plate with calpain as the substrate for 1 h at 37 °C. The fluorescence intensity (Ex/Em = 400/505 nm) of the samples was measured using a fluorescent microplate reader (BioTek, Santa Clara, CA, USA). Active calpain 1 and calpain inhibitors were used as positive and negative controls, respectively.

Statistical Analysis: Results were expressed as mean ± SEM. Analysis between more than two sample groups was performed by a one-way unstacked ANOVA and post-hoc LSD testing. Analysis between two paired samples was performed by a two-tailed unpaired Student's *t*-test. *P* values less than 0.05 were considered statistically significant.

Supporting Information

Supporting Information is available from the Wiley Online Library or from the author.

Acknowledgements

Conflict of Interest

The authors declare no conflict of interest.

Data Availability Statement

The data that support the findings of this study are available from the corresponding author upon reasonable request.

[1] M. G. Tonnesen, X. Feng, R. A. F. Clark, *J. Investig. Dermatol. Symp. Proc.* **2000**, *5*, 40.

[2] A. Laurenzana, G. Fibbi, F. Margheri, A. Biagioni, C. Luciani, M. Rosso, A. Chilla, *Curr. Mol. Med.* **2015**, *15*, 606.

[3] C. Korn, H. G. Augustin, *Dev. Cell* **2015**, *34*, 5.

[4] L. A. Dipietro, *Curr. Opin. Rheumatol.* **2013**, *25*, 87.

[5] J. Chen, L. E. H. Smith, *Angiogenesis* **2007**, *10*, 133.

[6] J. M. Tarr, K. Kaul, M. Chopra, E. M. Kohner, R. Chibber, *ISRN Ophthalmol.* **2013**, *2013*, 343560.

[7] L. A. Dipietro, *J. Leukocyte Biol.* **2016**, *100*, 979.

[8] S. Li, A. Hafeez, F. Noorulla, X. Geng, G. Shao, C. Ren, G. Lu, H. Zhao, Y. Ding, X. Ji, *Prog. Neurobiol.* **2017**, *157*, 79.

[9] E. C. De Heer, M. Jalving, A. L. Harris, *J. Clin. Invest.* **2020**, *130*, 5074.

[10] Y. Zhai, K. Schilling, T. Wang, M. El Khatib, S. Vinogradov, E. B. Brown, X. Zhang, *Biomaterials* **2021**, *276*, 121041.

[11] Y. Kang, S. Kim, M. Fahrenholtz, A. Khademhosseini, Y. Yang, *Acta Biomater.* **2013**, *9*, 4906.

[12] N. G. Schott, N. E. Friend, J. P. Stegemann, *Tissue Eng., Part B* **2021**, *27*, 199.

[13] K. Pill, S. Hofmann, H. Redl, W. Holnthoner, *Cell Regener.* **2015**, *4*, 8.

[14] C. Cao, Y. Huang, Q. Tang, C. Zhang, L. Shi, J. Zhao, L. Hu, Z. Hu, Y. Liu, L. Chen, *Biomaterials* **2018**, *172*, 1.

[15] Y. Cao, Y. Gong, L. Liu, Y. Zhou, X. Fang, C. Zhang, Y. Li, J. Li, *J. Appl. Toxicol.* **2017**, *37*, 1359.

[16] Y. H. Kim, J. Choi, M. J. Yang, S. P. Hong, C.-K. Lee, Y. Kubota, D.-S. Lim, G. Y. Koh, *Nat. Commun.* **2019**, *10*, 838.

[17] Y. Ravichandran, B. Goud, J.-B. Manneville, *Curr. Opin. Cell Biol.* **2020**, *62*, 104.

[18] D. M. Bryant, A. S. Yap, *Traffic* **2016**, *17*, 1231.

[19] B. Coxam, A. Sabine, N. I. Bower, K. A. Smith, C. Pichol-Thievend, R. Skoczylas, J. W. Astin, E. Frampton, M. Jaquet, P. S. Crosier, R. G. Parton, N. L. Harvey, T. V. Petrova, S. Schulte-Merker, M. Francois, B. M. Hogan, *Cell Rep.* **2014**, *7*, 623.

[20] R. Mayor, S. Etienne-Manneville, *Nat. Rev. Mol. Cell Biol.* **2016**, *17*, 97.

[21] M.-C. Lebart, Y. Benyamin, *FEBS J.* **2006**, *273*, 3415.

[22] Y. Zhang, N. M. Liu, Y. Wang, J. Y. Youn, H. Cai, *Biochim. Biophys. Acta, Mol. Basis Dis.* **2017**, *1863*, 1326.

[23] T. Alon, I. Hemo, A. Itin, J. Pe'er, J. Stone, E. Keshet, *Nat. Med.* **1995**, *1*, 1024.

[24] M. F. Brizzi, P. Defilippi, *Transl. Lung Cancer Res.* **2013**, *2*, 466.

[25] F. T. Zahra, E. Choleva, Md. S. Sajib, E. Papadimitriou, C. M. Mikelis, *Methods Mol. Biol.* **2019**, *1952*, 211.

[26] F. Tetzlaff, A. Fischer, *Bio-Protoc.* **2018**, *8*, e2995.

[27] G. A. Strasser, J. S. Kaminker, M. Tessier-Lavigne, *Blood* **2010**, *115*, 5102.

[28] R. Del Toro, C. Prahst, T. Mathivet, G. Siegfried, J. S. Kaminker, B. Larrivee, C. Breant, A. Duarte, N. Takakura, A. Fukamizu, J. Penninger, A. Eichmann, *Blood* **2010**, *116*, 4025.

[29] M. J. Siemerink, I. Klaassen, I. M. C. Vogels, A. W. Griffioen, C. J. F. Van Noorden, R. O. Schlingemann, *Angiogenesis* **2012**, *15*, 151.

[30] P. Nowak-Sliwinska, K. Alitalo, E. Allen, A. Anisimov, A. C. Aplin, R. Auerbach, H. G. Augustin, D. O. Bates, J. R. Van Beijnum, R. H. F. Bender, G. Bergers, A. Bikfalvi, J. Bischoff, B. C. Böck, P. C. Brooks, F. Bussolino, B. Cakir, P. Carmeliet, D. Castranova, A. M. Cimpean, O. Cleaver, G. Coukos, G. E. Davis, M. De Palma, A. Dimberg, R. P. M. Dings, V. Djonov, A. C. Dudley, N. P. Dufton, S.-M. Fendt, et al, *Angiogenesis* **2018**, *21*, 425.

[31] L. Claesson-Welsh, *Upsala J. Med. Sci.* **2015**, *120*, 135.

[32] R. S. Udan, T. J. Vadakkan, M. E. Dickinson, *Development* **2013**, *140*, 4041.

[33] A. Meeson, M. Palmer, M. Calfon, R. Lang, *Development* **1996**, *122*, 3929.

[34] A.-C. Vion, T. Perovic, C. Petit, I. Hollfinger, E. Bartels-Klein, E. Frampton, E. Gordon, L. Claesson-Welsh, H. Gerhardt, *Front Physiol.* **2020**, *11*, 623769.

[35] Q. Liu, M. Li, S. Wang, Z. Xiao, Y. Xiong, G. Wang, *Front. Cell Dev. Biol.* **2020**, *8*, 601224.

[36] N. Jaiswal, S. E. Haynesworth, A. I. Caplan, S. P. Bruder, *J. Cell. Biochem.* **1997**, *64*, 295.

[37] M. Pranskunas, E. Šimoliūnas, M. Alksne, V. Martin, P. S. Gomes, A. Puisys, A. Kaupinis, G. Juodzbalys, *Materials* **2021**, *14*, 3512.

[38] E. Komiya, H. Sato, N. Watanabe, M. Ise, S. Higashi, Y. Miyagi, K. Miyazaki, *Cancer Med.* **2014**, *3*, 537.

[39] V. Hwa, Y. Oh, R. G. Rosenfeld, *Endocr. Rev.* **1999**, *20*, 761.

[40] L. Jin, F. Shen, M. Weinfeld, C. Sergi, *Front. Oncol.* **2020**, *10*, 727.

[41] D. Chen, B. K. Yoo, P. K. Santhekadur, R. Gredler, S. K. Bhutia, S. K. Das, C. Fuller, Z.-Z. Su, P. B. Fisher, D. Sarkar, *Clin. Cancer Res.* **2011**, *17*, 6693.

[42] K. Tamura, M. Yoshie, K. Hashimoto, E. Tachikawa, *J. Reprod. Dev.* **2014**, *60*, 447.

[43] Y. Sun, W. Chen, R. J. Torphy, S. Yao, G. Zhu, R. Lin, R. Lugano, E. N. Miller, Y. Fujiwara, L. Bian, L. Zheng, S. Anand, F. Gao, W. Zhang, S. E. Ferrara, A. E. Goodspeed, A. Dimberg, X.-J. Wang, B. H. Edil, C. C. Barnett, R. D. Schulick, L. Chen, Y. Zhu, *Sci. Transl. Med.* **2021**, *13*, 604.

[44] M. E. Piroli, J. O. Blanchette, E. Jabbarzadeh, *Front. Biosci.-Landmark* **2019**, *24*, 451.

[45] D. MacKay, A. L. Miller, *Altern. Med. Rev.* **2003**, *8*, 359.

[46] J. M. Reinke, H. Sorg, *Eur. Surg. Res.* **2012**, *49*, 35.

[47] X. Yao, S. M. Carleton, A. D. Kettle, J. Melander, C. L. Phillips, Y. Wang, *Ann. Biomed. Eng.* **2013**, *41*, 1139.

[48] Y. Hou, R. Qiao, F. Fang, X. Wang, C. Dong, K. Liu, C. Liu, Z. Liu, H. Lei, F. Wang, M. Gao, *ACS Nano* **2013**, *7*, 330.